Projected entangled pair states study of anisotropic-exchange magnets on the triangular lattice

Meng Zhang, Chao Wang, Shaojun Dong, Hao Zhang, Yongjian Han,* and Lixin He†
CAS Key Laboratory of Quantum Information and Synergetic Innovation Center of Quantum Information and Quantum Physics, University of Science and Technology of China, Hefei 230026, China

(Received 23 August 2021; revised 28 November 2021; accepted 3 January 2022; published 11 January 2022)

The anisotropic-exchange spin-1/2 model on the triangular lattice has been used to describe the rare-earth chalcogenides, which may have exotic ground states. We investigate the quantum phase diagram of the model by using the projected entangled pair state method, and compare it to the classical phase diagram. Besides two stripe-ordered phases, and the 120° phase, there is also a multi-**Q** phase. We identify the multi-**Q** phase as a Z_2 vortex state. No quantum spin liquid state is found in the phase diagram, contrary to the previous density matrix renormalization group calculations.

DOI: 10.1103/PhysRevB.105.024411

I. INTRODUCTION

Over the past few decades, frustrated magnets, which can host nontrivial order and exotic quantum phases, have attracted great attention. The nearest-neighbor triangular antiferromagnet is a typical example of geometric frustration magnets, where the lattice geometry precludes simultaneous minimization of the energies of all bonds. Anderson proposed that the ground state of the model is a quantum spin liquid (QSL) state [1,2]. However, numerical calculations show that the ground state is instead a 120° order state [3,4].

The bond-dependent anisotropic exchange can be an alternative approach to enhance the frustration effects, which may lead to exotic quantum magnetic states. A famed example is the Kitaev spin model on the honeycomb lattice [5], where each bond with different spatial orientation carries a different Ising-like interaction. An exact solution of this model shows that the ground state is a QSL state with fractional spin excitations. Very recently, a large family of rare-earth triangular lattice materials, including $YbMgGaO_4$ [6–13] and rare-earth chalcogenide family $NaYbCh_2$ (Ch = O, S, Se) [14,15], have been synthesized and explored experimentally. In these materials, Yb^{3+} ions form a perfect triangular layer with effective spin-1/2 local moments. Strong spin-orbit coupling (SOC) introduces the anisotropic spin interactions, which provides ideal platforms to explore the interplay of bond-dependent exchange frustration and geometric frustration. Experimentally [6–15], it has been demonstrated that these rare-earth materials show no long-range magnetic order down to low temperature, which have been proposed as promising candidates as quantum spin liquids.

To understand the magnetic properties of the triangular materials, a generic spin-1/2 spin model with anisotropic exchange interactions on triangular lattice based on symmetry consideration has been proposed in Refs. [8,16]. This model reduces to the Kitaev-Heisenberg (KH) model for certain exchange parameters. Despite the model has been studied intensively by various numerical and theoretical methods, including the classical spin method [17–20], mean-field theory [7,21], exact diagonalization (ED) [22], and density matrix renormalization group (DMRG) method [17,23,24], the phase diagram of the model is still illusive. Specifically, DMRG calculations [17,23], as well as ED [22] calculations on small clusters, show that there is a QSL region between the stripe phases and the 120° phase. However, the QSL state calculated by ED has a different parent state than that of the DMRG result [23]. Meanwhile other DMRG [25] studies on the KH model show that this region in the phase diagram actually has a Z_2 vortex ground state, instead of QSL. It is therefore very urgent and important to know whether there is indeed a QSL region in the phase diagram.

To clarify the phase diagram of the anisotropic exchange spin-1/2 model on the triangular lattice, we perform high accuracy projected entangled pair states (PEPS) calculations, and compare the results to those of the classical simulations. We explore the phase diagram of the model, and find the stripe phases, 120° phase, and multi-**Q** phase in both quantum and classical models. Most importantly, we identify that the multi-**Q** phase, between the stipe orders and the 120° phase, is a Z_2 vortex state, which would *not* melt to QSL by quantum fluctuation.

The rest of the paper is organized as follows. In Sec. II, we introduce the anisotropic exchange model on the triangular lattice, and the methods used in this work. We present the phase diagram of the classical simulations in Sec. III A and the phase diagram of the quantum model in Sec. III B. We discuss more on the Z_2 vortex state in Sec. III C and summarize the work in Sec. IV.

II. MODEL AND METHODS

The generic nearest-neighbor spin-1/2 Hamiltonian, which is invariant under symmetry group $R\bar{3}m$, can be written as

*smhan@ustc.edu.cn
†helx@ustc.edu.cn

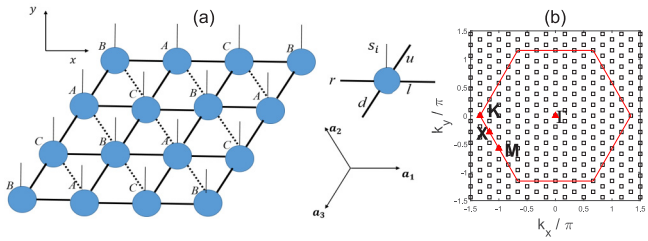

FIG. 1. (a) A schematic diagram of PEPS on a triangular lattice. The thick solid lines represent the virtual bonds of the PEPS, whereas the thin vertical lines are the physical indices of the PEPS. "*A*," "*B*," and "*C*" in the figure denote the three sublattices of the triangular lattice. $\varphi_\alpha = \{0, 2\pi/3, -2\pi/3\}$ for the bond along the primitive vectors $\mathbf{a}_1$, $\mathbf{a}_2$, and $\mathbf{a}_3$, respectively. (b) The Brillouin zone of the triangular lattice, where the squares denote the $\mathbf{k}$ points of a 12×12 lattice. Γ, K, M are the high symmetric points in the Brillouin zone, and the X point is located on the line between the K and M points.

[8,16]

$$\mathcal{H} = \sum_{\langle ij \rangle} \Big\{ J\big(S_i^x S_j^x + S_i^y S_j^y + \Delta S_i^z S_j^z\big) + 2J_{\pm\pm}\big[\big(S_i^x S_j^x - S_i^y S_j^y\big)\cos\varphi_\alpha - \big(S_i^x S_j^y + S_i^y S_j^x\big)\sin\varphi_\alpha\big] + J_{z\pm}\big[\big(S_i^y S_j^z - S_i^z S_j^y\big)\cos\varphi_\alpha - \big(S_i^x S_j^z + S_i^z S_j^x\big)\sin\varphi_\alpha\big]\Big\}. \tag{1}$$

Here S_i refers to the spin-1/2 operators on site i, and $\langle ij \rangle$ denotes a pair of nearest-neighbor spins. $\varphi_\alpha = \{0, 2\pi/3, -2\pi/3\}$ are the angles between the lattice vectors $\mathbf{a}_\alpha$ and the x axis [see Fig. 1(a)] in crystallographic axes. The first term of Eq. (1) is the standard XXZ model and is invariant under the global spin rotation around the z axis. The $J_{\pm\pm}$ and $J_{z\pm}$ terms define the bond-dependent anisotropic interactions caused by the strong SOC, which break the rotational symmetries of the Hamiltonian, but retain the time reversal symmetry. In this work, we set $J = 1$, and $J_{z\pm}$ take positive values, because the phase diagram for $-J_{z\pm}$ can be obtained by a global π rotation around the z axis [16].

It is also natural to rewrite model (1) in the cubic axes. When $\Delta = 1$ and $J_{z\pm} = 2\sqrt{2}J_{\pm\pm}$, model (1) is reduced to the well-known KH model in the cubic axes [17]. More details of the relation between model (1) and the KH model are given in Appendix A1. Recent first-principles calculations show that Δ is rather close to 1 in $NaYbS_2$ ($\Delta = 0.980$) and $NaYbO_2$ ($\Delta = 0.889$) [26]. Therefore, in this work, we focus on the phase diagram in the case of $\Delta = 1$.

We investigate the anisotropic triangular model (1), by using both the classical method and the quantum many-particle method. In the classical simulations, the spins are treated as unimodular classical vectors. We obtain the ground state of the classical model on a 30×30 lattice by optimizing the total energies via a replica exchange molecular spin dynamics method [27–29], which can effectively avoid the system being trapped in the local minima.

To investigate the phase diagram of the quantum model, we employ the PEPS method. The ground state wave functions are presented by PEPS on the $N = L_x \times L_y$ triangular lattices with open boundary conditions, as schematically shown in Fig. 1(a),

$$|\Psi\rangle = \sum_{s_1 \cdots s_N = 1}^{d} \mathrm{Tr}\big(A_1^{s_1} A_2^{s_2} \cdots A_N^{s_N}\big)|s_1 s_2 \cdots s_N\rangle, \tag{2}$$

where tensor $A_i^{s_i} = A_i(r, l, u, d, s_i)$ is a five-index tensor located on site i. s_i is the physical index and r, l, u, d are the virtual bonds of the PEPS, with a bond dimension D. In this study, all results are obtained by the PEPS with $D = 8$, unless otherwise noted. To obtain a highly accurate ground state, the PEPS wave functions are first optimized by the imaginary time evolution with a simple update method [30], followed by a stochastic gradient optimization method [31].

To distinguish different ordered states, we calculate the spin structure factor (SSF) for each spin component,

$$S^\nu(\mathbf{q}) = \frac{1}{N}\sum_{ij} e^{i\mathbf{q}\cdot(\mathbf{R_i}-\mathbf{R_j})}\big\langle S_i^\nu S_j^\nu\big\rangle, \tag{3}$$

where $\nu = x, y, z$ are the spin components and N is the total number of sites. The total SSF is the sum of the three components. In Fig. 1(b), we show the Brillouin zone of the 12×12 triangular lattice, where the X point is located on the line between the K and M points.

III. RESULTS AND DISCUSSION

A. Phase diagram of the classical model

The phase diagram of the classical simulations in the $J_{z\pm}$-$J_{\pm\pm}$ plane is shown in Fig. 2(a) for Δ=1. There are five different phases. On the left side of the phase diagram, the ground state is of a stripe-x order, where the spins lie in the x-y plane. In the top-right corner of the phase diagram, there is another stripe-ordered phase, the stripe-yz phase, where the spins are partially out of the x-y plane. In the vicinity of $J_{z\pm}, J_{\pm\pm} \sim 0$, there is the 120° phase. The spin textures of the 120°, stripe-x and stripe-yz phases are shown in Figs. 2(b)–2(d), respectively. All these states are single-**Q** commensurate states.

In the intermediate region of the phase diagram, multi-**Q** phases become the ground states, in which the magnetic moments are ordered at multiple **Q** vectors in the Brillouin zone. One of the multi-**Q** phases, which surrounds the 120° phase, is the modulated 120° phase. The noncoplanar spin configuration of the modulated 120° phase remains close to the 120° configuration locally, but modulates at larger scale, as shown in Fig. 2(e). The typical total SSF of the (classical) modulated 120° phase is given in Fig. 10(a) of Appendix A 3, which shows that the peaks of the total SSF move slightly away from the wave vector K point, which is the ordering vector of the 120° state.

In addition to the modulated 120° phase, there is another multi-**Q** phase, which can be identified as a Z_2 vortex state by its real-space spin textures and SSFs. In Figs. 3(a)–3(c), we plot the spin configurations in the three sublattices of a 30×30 lattice. The spin configurations of a given sublattice consist of ferromagnetic (FM) domains and vortices. In the region where one sublattice forms a FM domain, the spins of the other two sublattices form vortices. More specifically, when we trace a closed path around the center of the FM

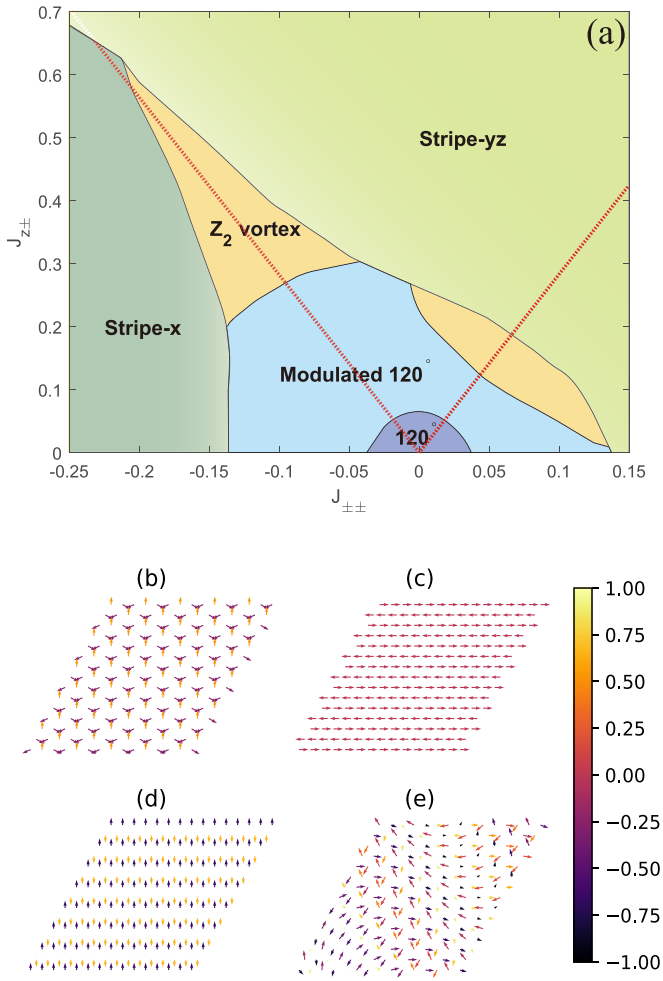

FIG. 2. (a) Classical phase diagram for model (1). On the red dotted line ($J_{z\pm} = \pm 2\sqrt{2}J_{\pm\pm}$), the anisotropic spin model (1), reduces to the KH model. (b)–(e) The spin configurations of (b) the 120° phase, (c) the stripe-x phase, (d) the stripe-yz phase, and (e) the modulated 120° phase. The arrows correspond to the projections of the classical spins onto the x-y plane, whereas the color of spins indicates the magnitude of S_z.

domain, the spins of the other two sublattices complete a 2π rotation around the center, i.e., the spin texture forms Z_2 vortices. The parent state of the Z_2 vortex state is also the 120° state, which has a similar local structure to the 120° state, but forms a vortex on large scale.

When $\Delta = 1$ and $J_{z\pm} = \pm 2\sqrt{2}J_{\pm\pm}$ [i.e., the two red lines in Fig. 2(a)], model(1) reduces to the KH model in the cubic axes [17], which has been extensively studied by various numerical methods [18,19,32]. It has been shown that there is a Z_2 vortex state in both the positive and the negative Kitaev interactions region of the KH model, which corresponds to the positive and negative $J_{\pm\pm}$ regions in Fig. 2(a). To compare our results with those of the KH model, we transform the spin configuration of the Z_2 vortex phase from the crystallographic reference frame to the cubic frame [17] and recalculate the SSFs of different spin components. Figure 3(d) shows the total SSF, whereas Figs. 3(e)–3(g) show the SSFs of the x, y, and z spin components, respectively. The peaks of the SSFs of the three spin components move slightly away from the K points along different directions. The SSFs are essentially the same with those of the Z_2 vortex phase in the KH model [18,19]. The results suggest that the Z_2 state is stable in a quite large parameter space beyond the KH model.

The anisotropic triangular spin model has been studied via the instabilities of magnons [17]. Reference [17] also finds a multi-**Q** phase in the case of $\Delta = 1$, in which the magnon spectra are softened at three symmetric **k** points in the immediate vicinity of the Γ and K points. The phase has been identified as the Z_2 phase. However, in Ref. [17], the multi-**Q** phase is proposed as a single Z_2 vortex state, in contrast to our results that there is also a modulated 120° state. Furthermore, in Ref. [17], the magnons of the 120° phase at $\Delta = 1$ are unstable to any finite value of $J_{z\pm}$, which is in contrast to our results that the 120° phase is stable when the anisotropic interactions $J_{z\pm}$ and $J_{\pm\pm}$ are small.

B. Phase diagrams of quantum model

In this section, we investigate the phase diagram of the anisotropic triangular model quantum mechanically to understand the effects of quantum fluctuation. The phase diagram is shown in Fig. 4 for $\Delta = 1$. Similar to the classical model, the stripe-x phase and the stripe-yz phase are on the bottom-left and top-right corner, respectively. In the intermediate region, there is a 120° phase and a multi-**Q** phase.

The phase diagram is determined by the order parameters $M(\mathbf{Q}) = \sqrt{\sum_\nu S^\nu(\mathbf{Q})/N}$, where S^ν ($\nu = x, y, z$) is the νth SSF of the spin component, and **Q** is the spin ordering vector. The typical total SSFs for the 120°, the stripe, and the multi-**Q** states on the 12×12 lattice are shown in Fig. 7. The SSFs of the 120° phase have peaks at the $\mathbf{Q} = K$ point, whereas the SSFs of the stripe phases have peaks at the M point. The SSF of a multi-**Q** phase has peaks around the X point, which lies in line between the M and K points. The details to determine the phase boundaries are given in Appendix A 2.

The stripe orders are trivial, and therefore will not be discussed further in the paper. We will focus on the multi-**Q** phase and the 120° phase in more detail.

Multi- **Q** *(Z_2 vortex) phase*. In Sec. III A, we identify that the multi-**Q** phase of the classical model with large anisotropic interaction is a Z_2 vortex state. To further determine the nature of the quantum state, we plot the SSFs of the quantum state in Figs. 5(a)–5(c) for the x, y, and z spin components at $J_{\pm\pm} = -0.1, J_{z\pm} = 0.325$ on a 15×15 lattice, respectively. We compare the SSFs with those of the classical model shown in Figs. 5(d)–5(f). Both results are computed in the crystallographic reference frame. The SSFs of the x, y, and z components show that the primary peaks of the quantum state are essentially the same as those of the classical model, i.e., the x, y components of the SSFs are asymmetric with respect to the Γ-M line, whereas the z component is symmetric with respect to this line. Similar results were also reported for a Z_2 vortex state in a DMRG study of the KH model [25]. These results suggest that this multi-**Q** state is also a Z_2 vortex state.

We note that previous DMRG calculations find a possible QSL phase in the region of $J_{z\pm} \simeq [0.27, 0.45]$ and $J_{\pm\pm} \simeq [-0.17, 0.1]$ in the isotropic limit $\Delta = 1$ [17,23], in contrast to the Z_2 vortex state obtained in this work. We note that the DMRG calculations were performed on rather narrow

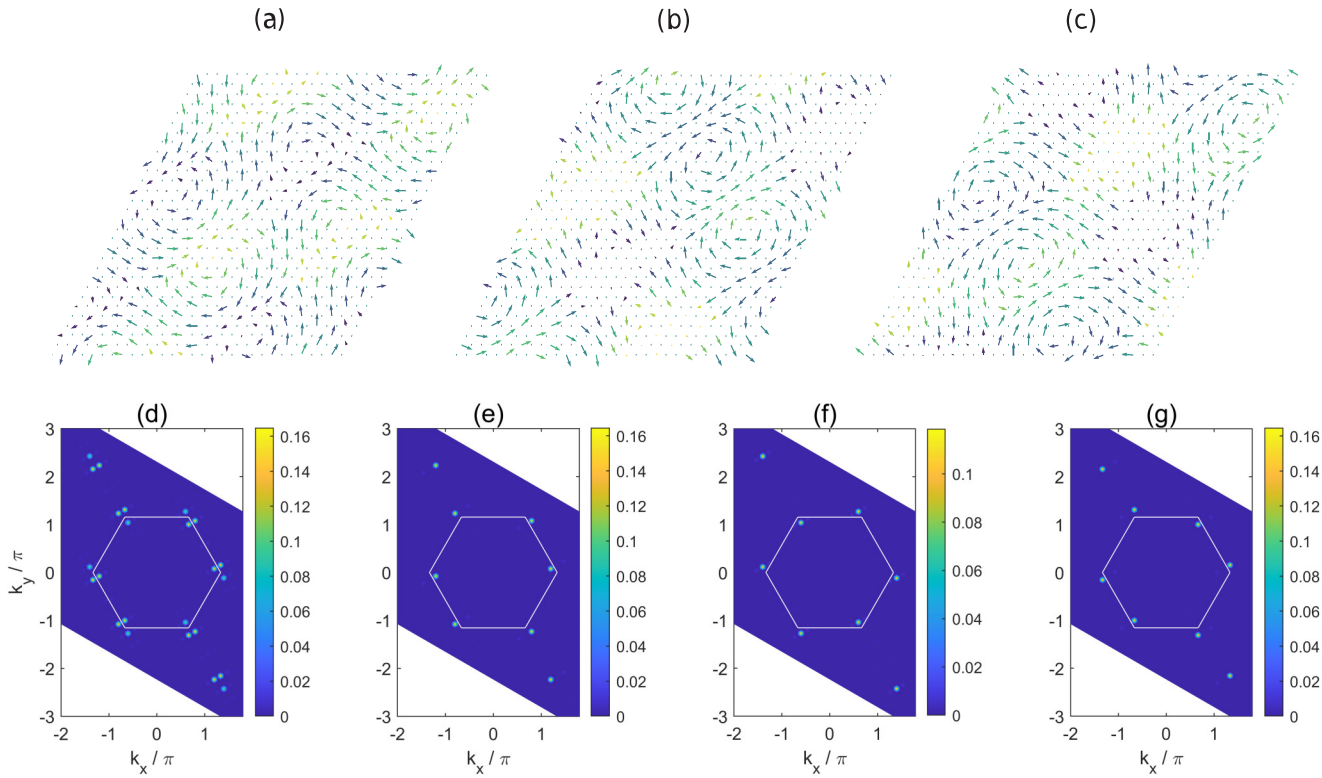

FIG. 3. Spin configurations and SSFs of the classical Z_2 vortex phase. (a)–(c) The spin configurations of three sublattices, where the spins have been projected onto the x-y plane, and the yellow arrows point upwards out of the plane and blue arrows point downwards out of the plane. (d) The total SSF of the Z_2 vortex phase, calculated at $J_{\pm\pm} = -0.1$, $J_{z\pm} = 0.325$ in the cubic axes, and (e)–(g) the SSFs of the x, y, and z components.

cylinders. To further check the stability of the Z_2 vortex phase in this region, we perform more detailed calculations using $J_{\pm\pm} = -0.1$, $J_{z\pm} = 0.325$, which is in the center of the possible QSL phase in previous DMRG studies [23], on larger lattices. Figures 6(a)–6(c) depict the total SSFs obtained by PEPS with $D = 8$ for the 15×15, 15×18, and 18×18 lattices, respectively. As we see, the SSFs show even sharper peaks around the K points for the larger lattice. Figures 6(d) and 6(e) show $M(\mathbf{Q})$, the intensity of the primary peaks of the

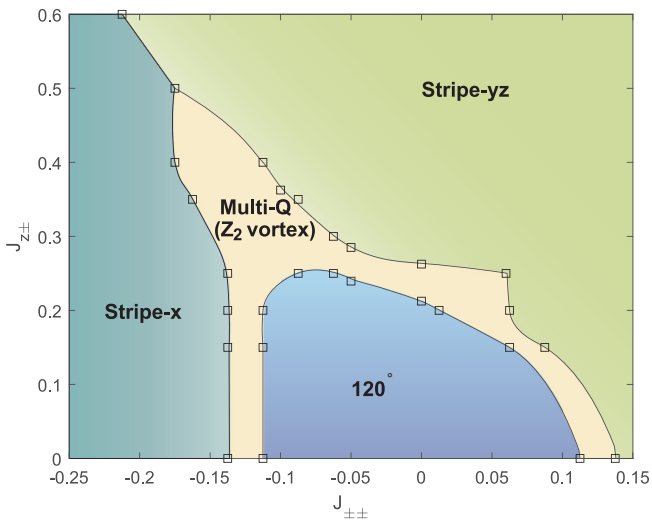

FIG. 4. The quantum phase diagram for model (1), including the stripe-x, stripe-yx, 120°, and Z_2 vortex phases.

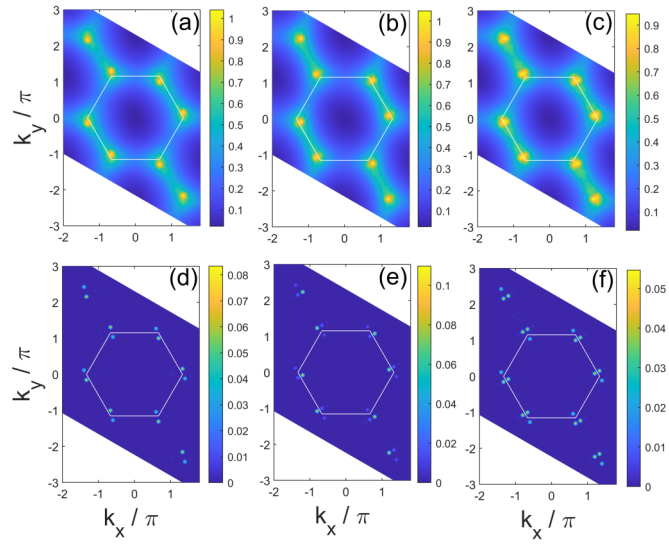

FIG. 5. The SSFs of the quantum and classical Z_2 vortex phases in the crystallographic axes. (a)–(c) The SSFs of the x, y, and z components of the quantum spin model at $J_{\pm\pm} = -0.1$, $J_{z\pm} = 0.325$, respectively. (d)–(f) The corresponding classical SSFs of the x, y, and z components at the same point.

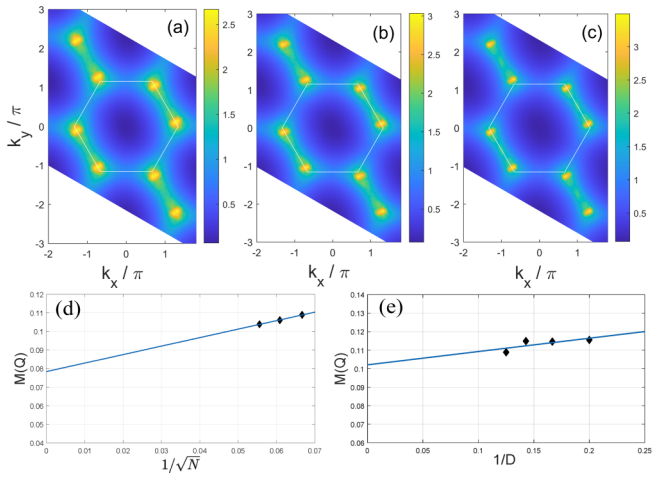

FIG. 6. The total SSFs of the quantum spin model at $J_{\pm\pm} = -0.1, J_{z\pm} = 0.325$ on the (a) 15×15 lattice, (b) 15×18 lattice, and (c) 18×18 lattice using bond dimension $D = 8$. (d) The intensity $M(\mathbf{Q})$ of the primary peaks as a function of $1/\sqrt{N}$ for $N = 15 \times 15$, 15×18, and 18×18. (e) $M(\mathbf{Q})$ as a function of $1/D$ for $D = 5, 6, 7, 8$ on the 15×15 lattice. Extrapolations are performed using linear fittings.

Z_2 vortex state, as functions of $1/\sqrt{N}$ and $1/D$, respectively. A finite-size extrapolation shows that $M(\mathbf{Q})$ still exists in the thermodynamic limit, and $M(\mathbf{Q})$ varies mildly with bond dimension D (see also Fig. 9 for SSFs obtained by PEPS with $D = 5$, 6, and 7 in the Appendix), which is finite as $D \to \infty$. These results suggest that the Z_2 vortex phase is stable and does not show any traces of melting in larger systems or using larger bond dimensions. Therefore, we conclude that model (1) has no QSL ground state or has only a very small QSL region in the phase diagram.

120° *phase*. The most noticeable difference between the phase diagrams of the classical model and quantum model, is that the modulated 120° phase disappears in the quantum model, and the region of the 120° phase is much larger than that of the classical model. The (classical) spin wave results also show that magnons in the $\Delta = 1$ limit are unstable to any finite value of $J_{z\pm}$, but the DMRG results show that the 120° state is stable for $J_{z\pm} \leqslant 0.27$ [17]. However, we find that the 120° state in the large anisotropic interactions $J_{z\pm}$ and $J_{\pm\pm}$ region, becomes unstable for larger systems. In Figs. 10(b) and 10(c), we compare the total SSFs of the 12×12 and 15×15 lattices for $J_{\pm\pm} = -0.025$ and $J_{z\pm} = 0.225$. Comparing to the SSF of the 12×12 lattice, the primary peaks of the 15×15 lattice move away slightly from the K point. The results suggest that the region of the 120° phase region in thermodynamic limit is smaller than that shown in Fig. 4, calculated on the 12×12 lattice.

C. Discussion

The Z_2 vortex state is a distortion of its 120° parent state. The interplay of bond-dependent anisotropic exchange and geometric frustration is the key to induce the Z_2 vortex phase [33]. In the KH model, the distance between vortices increases with decreasing anisotropic Kitaev interaction. Therefore, in relatively small systems, the area of the Z_2 vortex phase is reduced, which suggests that a large system size is necessary to detect the Z_2 vortex state.

Our calculations show that the Z_2 vortex state is stable in the intermediate region between the 120° phase and the two stripe phases, and the quantum fluctuations would not destroy the classical Z_2 vortex state. This is contrary to the DMRG results which find a QSL phase in the region [17,23]. In the anisotropic triangular model, the large coordination numbers play vital roles to stabilize the classical magnetic orders, despite the existence of bond-dependent exchange frustration and geometric frustration [34].

The Z_2 vortex state can be detected by small-angle neutron or x-ray scattering methods and NMR. There are many materials that can be described by model (1), including rare-earth chalcogenide family $NaYbCh_2$ (Ch = O, S, Se) [14,15], $YbMgGaO_4$ [6–13], iridate $Ba_3IrTi_2O_9$, etc. These materials can serve as a potential platform to observe the Z_2 vortex state.

We note that some experimental studies have found some spin liquid signature in these materials, but our results suggest that the nearest-neighbor interaction model in the triangular lattice does not give rise to spin liquid phase. Additional interactions might be important to describe these materials; for instance, next nearest-neighbor interaction [26] or the interlayer interactions [15].

IV. SUMMARY

We investigate the phase diagram of the quantum anisotropic triangular model by using the PEPS method, and compare it to that of the classical model. The results show the quantum phase diagram is very similar to that of the classical model. We identify the multi-**Q** phase between the stripe phases and the 120° phase as the Z_2 vortex state, which is stable even under the quantum fluctuation. No quantum spin liquid state is found in the phase diagram, contrary to the previous DMRG calculations.

ACKNOWLEDGMENTS

This work is supported by the National Science Foundation of China (Grants No. 11774327 and No. 11874343). The numerical calculations have been done on the USTC HPC facilities.

APPENDIX

1. Kitaev-Heisenberg model

Many rare-earth magnets can support the Kitaev type of bond-dependent exchange interactions, including the materials of the honeycomb lattice, triangular lattice and pyrochlore lattice built from edge-sharing octahedra [35,36]. In the rare-earth compounds, such as $YbMgGaO_4$ and $NaYbCh_2$ (Ch = O, S, Se), the layered triangular lattice structures are composed of magnetic ions surrounded by edge-sharing octahedra of ligands. The bonds of magnetic ions and ligands form cubic shapes [17,35]. Following the choice of Ref. [17], the transformation from the cubic to crystallographic reference

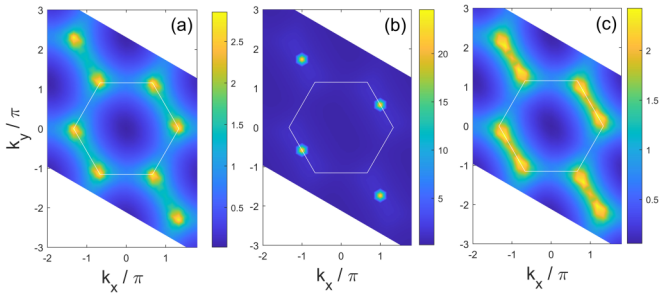

FIG. 7. Typical total SSFs of the quantum model of (a) the 120° phase at $J_{\pm\pm}=0, J_{z\pm}=0.15$; (b) the stripe phase yz at $J_{\pm\pm}=0.2, J_{z\pm}=0.2$, and (c) the multi-**Q** phase for $J_{\pm\pm}=-0.1, J_{z\pm}=0.25$. The results are calculated on a 12×12 lattice.

frame, $\mathbf{S}_{\text{cryst}}=\hat{\mathbf{R}}\mathbf{S}_{\text{cubic}}$, is given by

$$\hat{\mathbf{R}}=\begin{pmatrix} 0 & \frac{1}{\sqrt{2}} & \frac{1}{\sqrt{2}} \\ -\sqrt{\frac{2}{3}} & \frac{1}{\sqrt{6}} & -\frac{1}{\sqrt{6}} \\ -\frac{1}{\sqrt{3}} & -\frac{1}{\sqrt{3}} & \frac{1}{\sqrt{3}} \end{pmatrix}. \tag{A1}$$

The Hamiltonian (1) can be rewritten as the extended Kitaev-Heisenberg model:

$$\mathcal{H}=\sum_{\langle ij\rangle_\gamma}\left[J_0\mathbf{S}_i\cdot\mathbf{S}_j+KS_i^\gamma S_j^\gamma+\Gamma\left(S_i^\alpha S_j^\beta+S_i^\beta S_j^\alpha\right)\right.$$
$$\left.+\Gamma'\left(S_i^\gamma S_j^\alpha+S_i^\gamma S_j^\beta+S_i^\alpha S_j^\gamma+S_i^\beta S_j^\gamma\right)\right], \tag{A2}$$

where $\{\alpha,\beta,\gamma\}=\{y,z,x\}$, $\{z,x,y\}$, and $\{x,y,z\}$, for the X bond, Y bond, and Z bond, respectively, and $\{\text{X,Y,Z}\}\equiv\{\pm\mathbf{a}_1,\pm\mathbf{a}_2,\pm\mathbf{a}_3\}$. In the $\Delta=1$ limit, and along the line of $J_{z\pm}=2\sqrt{2}J_{\pm\pm}$, model (A2) reduces to the Kitaev-Heisenberg model,

$$\mathcal{H}=\sum_{\langle ij\rangle_\gamma}J_0\mathbf{S}_i\cdot\mathbf{S}_j+KS_i^\gamma S_j^\gamma, \tag{A3}$$

where $J_0=J+2J_{\pm\pm}$ and $K=-6J_{\pm\pm}$.

2. Phase boundary of the quantum model

The typical total SSFs of the 120° phase, stripe phases, and multi-**Q** phase are shown in Fig. 7 for the quantum spin model. The SSFs are calculated on a 12×12 lattice via the PEPS method. The SSFs are peaked at the K point, M point, and around the X point for the 120° phase, stripe phases, and multi-**Q** phases, respectively. The values of the peaks can be used as the order parameters of the phases.

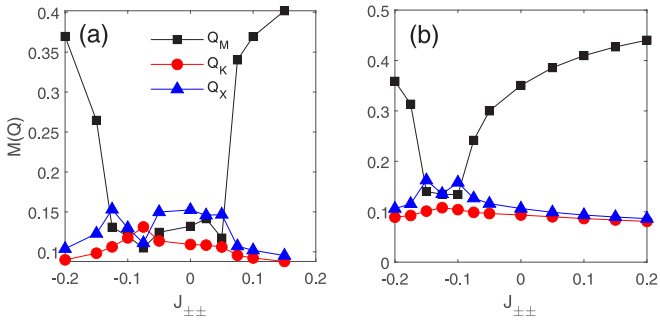

FIG. 8. The order parameters $M(\mathbf{Q})$ as functions of $J_{\pm\pm}$ with (a) $J_{z\pm}=0.25$ and (b) $J_{z\pm}=0.35$.

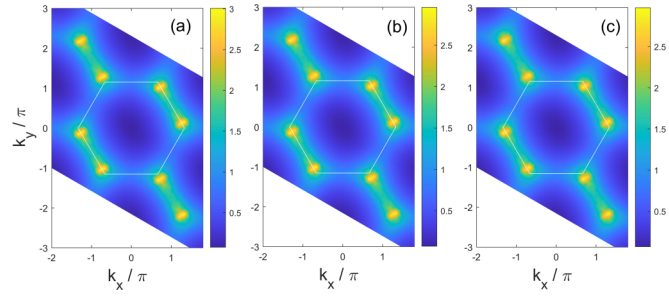

FIG. 9. The total SSFs obtained by PEPS with (a) $D=5$ and (b) $D=6$ and (c) $D=7$ for $J_{\pm\pm}=-0.1, J_{z\pm}=0.325$ on the 15×15 lattice.

To determine the phase boundary of the quantum model, we scan the parameters in the $J_{\pm\pm}$-$J_{z\pm}$ plane with $\Delta=1$, and calculate the order parameters. Figure 8 depicts the order parameters $M(\mathbf{Q})$ at $\mathbf{Q}=M, K, X$, as functions of $J_{\pm\pm}$ for $J_{z\pm}=0.25$ [Fig. 8(a)] and $J_{z\pm}=0.35$ [Fig. 8(b)], respectively. The results are obtained on the 12×12 lattice. These results suggest that the intermediate region of the phase diagram is multi-**Q** phase, which can be further identified as a Z_2 vortex phase. There are first-order-like phase transitions from the 120°/multi-**Q** phases to the stripe phases, which are consistent to previous DMRG study [23]. The phase boundary between the multi-**Q** phase and the two stripe phases is close to the boundary of classical results and classical spin-wave results [17].

3. Additional results

Figure 9 shows the total SSFs obtained by the PEPS with $D=5$, 6, and 7 in the Z_2 vortex phase, which are essentially the same as those obtained by using $D=8$ [see Fig. 6(a)]. Therefore, the PEPS with $D=8$ is large enough to capture the essential physics of the Z_2 vortex state.

Figure 10 depicts the total SSFs calculated at $J_{\pm\pm}=-0.025$ and $J_{z\pm}=0.225$. Figure 10(a) shows the SSF of the classical model calculated on a 30×30 lattice, whose peaks move slightly away from the K points. The SSF suggests that the ground state is a modulated 120° phase. Figures 10(b)

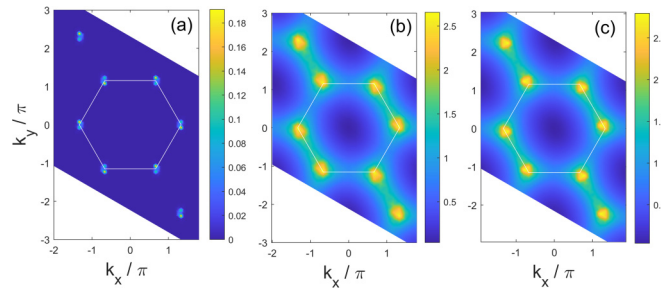

FIG. 10. The total SSFs calculated at $J_{\pm\pm}=-0.025, J_{z\pm}=0.225$: (a) the SSF of the classical model, and (b),(c) the SSFs of the quantum model calculated at the 12×12 and 15×15 lattices by PEPS, respectively.

and 10(c) depict the SSFs of the quantum model calculated by PEPS on the 12×12 and 15×15 lattices, respectively. For the 12×12 lattice, the peaks of the SSF are located on the K points, suggesting that the ground state is a 120° phase. However, the SSF of the 15×15 lattice is similar to that of the classical modulated 120° phase, whose primary peaks move slightly away from the K points, which means that the 120° phase is unstable at this point. Therefore, the region of the 120° phase should be smaller than that calculated on the 12×12 lattice in the thermodynamic limit.

[1] P. W. Anderson, Mater. Res. Bull. **8**, 153 (1973).
[2] P. W. Anderson, Science **235**, 1196 (1987).
[3] D. A. Huse and V. Elser, Phys. Rev. Lett. **60**, 2531 (1988).
[4] P. Sindzingre, P. Lecheminant, and C. Lhuillier, Phys. Rev. B **50**, 3108 (1994).
[5] A. Kitaev, Ann. Phys. **321**, 2 (2006).
[6] Y. Li, H. Liao, Z. Zhang, S. Li, F. Jin, L. Ling, L. Zhang, Y. Zou, L. Pi, Z. Yang, J. Wang, Z. Wu, and Q. Zhang, Sci. Rep. **5**, 16419 (2015).
[7] K. Li, S.-L. Yu, and J.-X. Li, New J. Phys. **17**, 043032 (2015).
[8] Y. Li, G. Chen, W. Tong, L. Pi, J. Liu, Z. Yang, X. Wang, and Q. Zhang, Phys. Rev. Lett. **115**, 167203 (2015).
[9] Y. Li, D. Adroja, P. K. Biswas, P. J. Baker, Q. Zhang, J. Liu, A. A. Tsirlin, P. Gegenwart, and Q. Zhang, Phys. Rev. Lett. **117**, 097201 (2016).
[10] Y. Li, D. Adroja, R. I. Bewley, D. Voneshen, A. A. Tsirlin, P. Gegenwart, and Q. Zhang, Phys. Rev. Lett. **118**, 107202 (2017).
[11] Y. Shen, Y.-D. Li, H. Wo, Y. Li, S. Shen, B. Pan, Q. Wang, H. C. Walker, P. Steffens, M. Boehm, Y. Hao, D. L. Quintero-Castro, L. W. Harriger, M. D. Frontzek, L. Hao, S. Meng, Q. Zhang, G. Chen, and J. Zhao, Nature (London) **540**, 559 (2016).
[12] J. A. M. Paddison, M. Daum, Z. Dun, G. Ehlers, Y. Liu, M. B. Stone, H. Zhou, and M. Mourigal, Nat. Phys. **13**, 117 (2016).
[13] Y. Li, S. Bachus, B. Liu, I. Radelytskyi, A. Bertin, A. Schneidewind, Y. Tokiwa, A. A. Tsirlin, and P. Gegenwart, Phys. Rev. Lett. **122**, 137201 (2019).
[14] W. Liu, Z. Zhang, J. Ji, Y. Liu, J. Li, X. Wang, H. Lei, G. Chen, and Q. Zhang, Chinese Phys. Lett. **35**, 117501 (2018).
[15] M. M. Bordelon, E. Kenney, C. Liu, T. Hogan, L. Posthuma, M. Kavand, Y. Lyu, M. Sherwin, N. P. Butch, C. Brown, M. J. Graf, L. Balents, and S. D. Wilson, Nat. Phys. **15**, 1058 (2019).
[16] Y.-D. Li, X. Wang, and G. Chen, Phys. Rev. B **94**, 035107 (2016).
[17] P. A. Maksimov, Z. Zhu, S. R. White, and A. L. Chernyshev, Phys. Rev. X **9**, 021017 (2019).
[18] M. Becker, M. Hermanns, B. Bauer, M. Garst, and S. Trebst, Phys. Rev. B **91**, 155135 (2015).
[19] I. Rousochatzakis, U. K. Rössler, J. van den Brink, and M. Daghofer, Phys. Rev. B **93**, 104417 (2016).
[20] C. Liu, R. Yu, and X. Wang, Phys. Rev. B **94**, 174424 (2016).
[21] P. Kos and M. Punk, Phys. Rev. B **95**, 024421 (2017).
[22] M. Wu, D.-X. Yao, and H.-Q. Wu, Phys. Rev. B **103**, 205122 (2021).
[23] Z. Zhu, P. A. Maksimov, S. R. White, and A. L. Chernyshev, Phys. Rev. Lett. **120**, 207203 (2018).
[24] Q. Luo, S. Hu, B. Xi, J. Zhao, and X. Wang, Phys. Rev. B **95**, 165110 (2017).
[25] K. Shinjo, S. Sota, S. Yunoki, K. Totsuka, and T. Tohyama, J. Phys. Soc. Jpn. **85**, 114710 (2016).
[26] D.-Y. Zheng, Z.-X. Shen, M. Zhang, and L. He, arXiv:2104.09739.
[27] R. H. Swendsen and J.-S. Wang, Phys. Rev. Lett. **57**, 2607 (1986).
[28] W. Liu, C. Wang, Y. Li, Y. Lao, Y. Han, G.-C. Guo, Y.-H. Zhao, and L. He, J. Phys.: Condens. Matter **27**, 085601 (2015).
[29] C. Wang, M. Gong, Y. Han, G. Guo, and L. He, Phys. Rev. B **96**, 115119 (2017).
[30] H. C. Jiang, Z. Y. Weng, and T. Xiang, Phys. Rev. Lett. **101**, 090603 (2008).
[31] W.-Y. Liu, S.-J. Dong, Y.-J. Han, G.-C. Guo, and L. He, Phys. Rev. B **95**, 195154 (2017).
[32] M. Li, N. B. Perkins, and I. Rousochatzakis, Phys. Rev. Res. **1**, 013002 (2019).
[33] E. Seabrook, M. L. Baez, and J. Reuther, Phys. Rev. B **101**, 174443 (2020).
[34] S. Wang, Z. Qi, B. Xi, W. Wang, S.-L. Yu, and J.-X. Li, Phys. Rev. B **103**, 054410 (2021).
[35] J. G. Rau and M. J. P. Gingras, Phys. Rev. B **98**, 054408 (2018).
[36] C. Liu, Y.-D. Li, and G. Chen, Phys. Rev. B **98**, 045119 (2018).